Published in final edited form as:
Biochemistry. 2012 March 27; 51(12): 2539–2550. doi:10.1021/bi201857v.

Interaction of tau protein with model lipid membranes induces tau structural compaction and membrane disruption

Emmalee M. Jones[†], **Manish Dubey**[‡], **Phillip J. Camp**[†], **Briana C. Vernon**[†], **Jacek Biernat**[§,%], **Eckhard Mandelkow**[§,%], **Jaroslaw Majewski**[‡], and **Eva Y. Chi**[†,*]

[†]Department of Chemical and Nuclear Engineering, Center for Biomedical Engineering, University of New Mexico, Albuquerque, New Mexico, 87131

[‡]Lujan Neutron Scattering Center, Los Alamos National Laboratory, Los Alamos, New Mexico, 87545

[§]Max Planck Unit for Structural Molecular Biology, c/o DESY, Hamburg, Germany

[%]Center for Neurodegenerative Diseases (DZNE) and CAESAR Research Center, Bonn, Germany

Abstract

The misfolding and aggregation of the intrinsically disordered, microtubule-associated tau protein into neurofibrillary tangles is implicated in the pathogenesis of Alzheimer's disease. However, the mechanisms of tau aggregation and toxicity remain unknown. Recent work has shown that lipid membrane can induce tau aggregation and that membrane permeabilization may serve as a pathway by which protein aggregates exert toxicity, suggesting that the plasma membrane may play dual roles in tau pathology. This prompted our investigation to assess tau's propensity to interact with membranes and to elucidate the mutually disruptive structural perturbations the interactions induce in both tau and the membrane. We show that although highly charged and soluble, the full-length tau (hTau40) is also highly surface active, selectively inserts into anionic DMPG lipid monolayers and induces membrane morphological changes. To resolve molecular-scale structural details of hTau40 associated with lipid membranes, X-ray and neutron scattering techniques are utilized. X-ray reflectivity indicates hTau40's presence underneath a DMPG monolayer and penetration into the lipid headgroups and tailgroups, whereas grazing incidence X-ray diffraction shows that hTau40 insertion disrupts lipid packing. Moreover, both air/water and DMPG lipid membrane interfaces induce the disordered hTau40 to partially adopt a more compact conformation with density similar to that of a folded protein. Neutron reflectivity shows that tau completely disrupts supported DMPG bilayers while leaving the neutral DPPC bilayer intact. Our results show that hTau40's strong interaction with anionic lipids induces tau structural compaction and membrane disruption, suggesting possible membrane-based mechanisms of tau aggregation and toxicity in neurodegenerative diseases.

Keywords

Alzheimer's disease; neutron reflectivity; x-ray grazing incidence diffraction; tau protein; lipid bilayers; protein-membrane interactions; tau aggregation

Alzheimer's disease (AD) is a neurodegenerative disease characterized by neurofibrillary tangles (NFTs) and amyloid plaques found in the brains of affected patients (1, 2). The

[*]Corresponding author Tel: 505.277.2263 evachi@unm.edu.

extracellular amyloid plaques consist of deposits of the amyloid-β peptide (Aβ) (3) and the intracellular NFTs are composed of aggregates of the hyperphosphorylated tau protein (4). In addition to AD, NFTs have also been linked to the pathogenesis of more than 20 other neurodegenerative disorders collectively termed tauopathies (5). Tau's role in the development of neurodegenerative diseases is still unclear, but a link between pathological tau aggregation and cognitive impairments has been shown (6). Moreover, the identification of multiple tau gene point mutations that result in hereditary tauopathies is evidence that tau malfunction alone is sufficient to cause neurodegeneration (7, 8). However, two key features of tau pathology are still unclear. First, the molecular basis of the early aggregation events, such as the structural fluctuations that trigger the aberrant accumulation of tau into NFTs rich in β-sheets *in vivo*, remains unknown. Second, the mechanism by which tau aggregation causes neuronal dysfunction is unclear.

Tau proteins are expressed primarily in the central nervous system, and their critical function of promoting microtubule (MT) assembly and stability is mediated by six isoforms, regulated by phosphorylation, which decreases tau's binding affinity to MT resulting in the disassociation of tau from MTs (2, 9, 10). Tau is rich in charged and hydrophilic residues and thus is highly soluble. In solution, tau is intrinsically disordered and, because of its high solubility, resistant to aggregation. In order to aggregate into fibrils, the intrinsically disordered tau needs to undergo conformational changes that render the protein aggregation-competent, or “pro-aggregant”. At present, the structure of the proaggregant form is unknown. However, the formation of β-sheet enriched fibrils from intrinsically disordered tau likely proceeds through the formation of partially folded, or structurally compact, conformations with increased aggregation propensities.

In vitro, the assembly of tau into β-sheet rich fibrils requires the addition of polyanionic cofactors, such as heparin and anionic micelles, suggesting that tau aggregation proceeds through a nucleation controlled polymerization pathway. The interactions between tau and the anionic inducers increase the protein's local concentration and compensate for its positive charges (11-15), both of which favor second or higher order reactions such as fibril formation. Whether the cofactors also induce conformational changes to the proteins, however, is unclear. At present, physiological factors and conditions that trigger tau fibril formation *in vivo* are still unknown.

Several lines of evidence suggest that plasma membranes may modulate tau aggregation. Tau has been shown to interact at least indirectly with the plasma membrane through its amino-terminal projection domain (Fig. 1A) (16) and is present in detergent resistant membrane microdomains (17, 18). Membrane glycolipids have been found to be associated with paired helical filaments (PHFs) isolated from AD brains (19). More recently, membrane associated chimeric tau has been shown to seed the formation of PHFs from full length tau protein (20) and anionic lipid vesicles have been shown to promote the aggregation of the MT binding domain of tau (K18) at sub- μM concentrations (21). Thus, plasma membrane mediated tau misfolding and aggregation may serve as an *in vivo* mechanism by which the protein nucleates and grows into PHFs. As such, even if the membrane bound tau is only a small fraction of the protein population, it may be capable of seeding the growth of mature fibrils.

Tau-mediated neurodegeneration can arise from the loss of physiological function and/or the gain-oftoxicity (22, 23). Tau aggregation abolishes its MT-stabilizing function and can impair axonal transport (24). However, the absence of significant neuronal abnormalities in tau knock-out mice suggests that tau's MT-stabilizing function may not be critical and that gain-of-toxicity is more likely. There is an ongoing debate as to whether mature tau fibrils are toxic or mere inert waste. The findings that a high β-propensity or “pro-aggregant” tau

leads both to tau aggregation and toxicity, whereas an "anti-aggregant" tau with no β-propensity is not toxic (25), suggest that aggregation is a key factor in neurodegeneration. However, the mechanism by which tau aggregates cause neuronal cell death is unknown. The roles of several other oligomeric protein aggregates have recently received considerable attention in numerous neurodegenerative diseases, including Aβ, α-synuclein, huntingtin, and prion oligomers (26-30). A leading hypothesis for the mechanism of protein aggregate-induced toxicity is cell membrane disruption, resulting in the alteration of ion homeostasis and disregulation of neuronal signal transduction (31-34). Increases in ion permeability have been found in cells exposed to various protein aggregates (35-38). Studies using model lipid membranes showed that Aβ induces either the formation of discrete ion channels (39, 40) or increases of bilayer conductance (31, 41, 42). Additionally, these types of membrane disruptions have been shown to be the molecular basis of cytotoxicity for naturally occurring antimicrobial peptides (43) and synthetic biocidal conjugated polyelectrolytes (44). Thus, disruption of the cell membrane may serve as a general pathway by which amphiphilic and membrane active macromoelcules exert cellular toxicity.

While the significance of the dual roles that the lipid membrane plays in tau pathology, catalyzing tau misfolding and aggregation into NFTs and serving as a target for tau aggregates to exert toxicity *via* membrane destabilization, has been recognized, the roles themselves are not well understood. At present, the interactions between lipid membranes and tau have not been well characterized, particularly the mutually disruptive structural perturbations the interactions induce in both tau and the membrane. The current study investigates the interactions between the recombinant full-length isoform of human tau protein (hTau40) (Fig. 1A) with two model lipid membranes: 1. lipid monolayer at the air/water interface, which models one leaflet of the plasma membrane, and 2. supported lipid bilayers, which better mimic the cell membrane. In particular, the current work focuses on elucidating the structural aspects of hTau40-membrane interactions. To probe tau-membrane interactions and investigate the effects of these interactions on tau conformation and membrane structural integrity, a combination of complementary biophysical techniques including pressure-area isotherms, fluorescence microscopy (FM), and *in situ* X-ray and neutron scattering techniques were utilized. We found that although highly charged and soluble, tau is also highly surface active and interacts strongly with anionic lipid membranes leading to structural compaction of the protein, which may render the protein "pro-aggregant", or aggregation-competent, and disruptions to membrane lipid packing, morphology, and structural integrity.

Materials and Methods

Materials

Full-length human tau isoform (hTau40, 441 residues) was synthesized and purified as previously described (45). Three lipids were used to evaluate the effect of lipid head group charge on tau-membrane interactions – zwitterionic 1,2-dimyristoyl-sn-glycero-3-phosphocholine (DMPC), anionic 1,2-dimyristoyl-sn-glycero-3-[phospho-rac-(1-glycerol)] (DMPG), and cationic 1,2-dimyristoyl-3-trimethylammonium-propane (DMTAP) (Fig. 1D). Zwitterionic 1,2-dipalmitoyl-snglycero-3-phosphocholine (DPPC) was used for neutron reflectivity experiments. All lipids were purchased from Avanti Polar Lipids and used as received. DMPC, DMTAP and DPPC were dissolved in chloroform ($CHCl_3$) (HPLC grade, Fisher Scientific) while DMPG was dissolved in 10 vol% methanol (MeOH) in chloroform. For FM, the headgroup-labeled fluorescent dye Texas Red 1,2-dihexadecanoyl 3-phosphoethanolamine (TR-DHPE) (Molecular Probes) was first dissolved in chloroform and subsequently added to lipid spreading solutions at 0.5 mol%. Lipid stock solutions ranged from 2 to 10 mg/ml were prepared and then diluted to 0.2 or 0.5 mg/mL for spreading solutions. All lipid solutions were stored at -20°C in glass vials.

Adsorption of hTau40 to air/water interface

To evaluate the surface activity of hTau40, the surface pressure (π) measured by the adsorption of hTau40 from a water subphase was measured. The experiment was carried out at 25°C and on a 45 mL water subphase (Milli-Q system, Millipore, Bedford, MA) using a MiniMicro Langmuir trough (KSV Instruments Ltd., Finland). A Wilhelmy plate sensor at the center of the trough measured π of the lipid monolayer where $\pi = \gamma_0 - \gamma$ and γ_0 is the air/water surface tension and γ is the lipid film surface tension. The trough had a working surface area of 86.39 cm^2. Before injecting hTau40 into the subphase, barriers were partially closed to give a total surface area of 45 cm^2, roughly the same as the surface area of the lipid monolayers compressed to 25 mN/m for the subsequent insertion experiments. For a final tau concentration of 1 μM, 1 mL of 45 μM tau was injected into the subphase using a gas tight glass microsyringe (Hamilton, Reno, NV).

Constant pressure insertion assay and fluorescence microscopy

To evaluate the interactions between hTau40 and lipid membranes, insertion of hTau40 into lipid monolayers at the air/water interface held at a constant π was measured. Figure 1B is a schematic of the insertion assay. All experiments were carried out on water subphase and at room temperature. Lipids were first spread at the air/water interface. The barriers then symmetrically compressed the monolayer at 0.3 mm/s to a target π of 25 mN/m and this π was kept constant *via* a feedback loop. A π of 25 mN/m was chosen for its relevance to physiological conditions as the lipid-packing density of a bilayer is reported to roughly correspond to that of a monolayer at ~30 mN/m (46, 47). The speed at which the barriers moved to maintain this target pressure was controlled by the feedback loop and depended upon how fast the barriers needed to expand or contract in response to a perturbation, for example, rate of tau insertion. A maximum barrier speed of 3 mm/min was set during the constant pressure duration of the experiment. Protein was then injected into the subphase underneath the monolayer to achieve a final 1 μM concentration. Since the monolayer was kept at a constant π, the barriers expanded as a result of protein insertion. Monolayer surface area was recorded and the % area expansion was taken as a measure of favorable tau-lipid interactions. Surface area expansion is defined as $\Delta A/A = (A\text{-}A_i)/A_i$, where A is the surface area at time t and A_i is the initial surface area of the monolayer when it reached 25 mN/m.

To monitor lipid monolayer morphological change during tau insertion, the trough was positioned on top of a motorized stage of an inverted optical microscope (Olympus IX 71) with a 50× objective centered on a quartz window in the bottom of the trough. A 100 Watt mercury lamp was used for fluorescence excitation. Fluorescence images were collected by a QImaging camera (EXi Blue, QImaging Photometrics) and analyzed using the software QCapture Pro. 0.5 mol% TR-DHPE was included in the spreading solution. Due to steric hindrance, the dye partitions into the liquid-expanded (LE) phase rather than the liquid-condensed (LC) phase, giving rise to fluorescence contrast (48).

X-Ray scattering measurements

Grazing-incidence X-ray diffraction (GIXD) and X-ray reflectivity (XR) data were collected at the BW1 beamline (HASYLAB, DESY, Hamburg, Germany) for both hTau40 adsorbed to the air/water interface and hTau40 inserted into a DMPG monolayer at the air/water interface. XR data give information about the out-of-plane (perpendicular to the lipid film) electron density profile of the film averaged over the LE and LC phases. GIXD measurements give structural information on the in-plane (i.e., in the plane of the monolayer) ordered (hence diffracting) portion of the film. Presence of Bragg peaks in GIXD data indicates 2D ordered structures. The theory of XR and GIXD has been presented in detail elsewhere (49, 50).

The synchrotron X-ray beam was monochromated to a wavelength (λ) of around 1.304 Å by Bragg reflection from a Beryllium (200) monochromator crystal in Laue geometry. By tilting the reflecting crystal planes out of the vertical plane the monochromatic beam was deflected down to impinge on the horizontal liquid surface at a shallow glancing angle. All experiments were carried out in an ultra-small volume Langmuir trough liquid diffractometer (20 mL subphase volume) at 23 °C and an hTau40 concentration of 1 μM in pure water. The trough was temperature controlled and equipped with a Wilhelmy balance for surface pressure measurements and a motorized barrier for surface area variation was mounted on the diffractometer. During the XR experiments at low incident angles, due to the small dimensions of the trough, the footprint of the beam was larger than the size of the trough. Therefore the normalized XR data was truncated to only include data at which the footprint of the incoming beam is smaller than the size of the trough.

For the XR experiments, reflectivity, R, is defined as the ratio of the intensity of X-rays specularly reflected from a surface relative to that of the incident X-ray beam measured as a function of wave-vector transfer ($Q_z=|\mathbf{k_{out}} - \mathbf{k_{in}}| = 4\pi\sin\theta/\lambda$, where θ is the grazing angle and λ is the wavelength of the X-ray beam). The R profile contains information on the sample-normal profile of in-plane average of the electron density. Chemically distinct molecular layers (e.g., proteins, lipid headgroups and tails) have different electron densities. Electron density profile of a film, therefore, gives us information on the location and thickness of the protein layer associated with the lipids (50, 51). The absolute R was derived by subtracting background followed by normalization to the incident beam flux. The data was reduced and plotted as R/R_F versus Q_z (the division by Fresnel reflectivity, R_F, increases the visibility of the reflectivity profile by removing a sharp Q_Z^{-4} decrease of the reflectivity due to Fresnel's law). The error bars on the data represent the statistical errors in the measurements (standard deviation, σR).

Analysis of the measured reflectivity profiles was performed using a free form StochFit fitting routine (52, 53). StochFit utilizes a stochastic procedure for analyzing XR data of thin films at an interface. StochFit first provides a model-independent electron density profile (ρ) of the XR data, after which ρ is fit with a box model with smeared interfaces to extract physically meaningful results (54). Each box represents a layer of distinct chemical composition, thus ρ. From the box model fitting, lengths, ρ normalized to that of water ρ_{H2O}, (ρ/ρ_{H2O}), and interfacial roughness values are reported for each box.

For the GIXD experiments, the X-ray beam was adjusted to strike the surface at an incident angle of 0.11°, which corresponds to a $q_z = 0.85\ Q_c$, where $Q_c = 0.02176\ Å^{-1}$ is the critical scattering vector for total external reflection from the liquid subphase. At this angle the incident wave is totally reflected, while the refracted wave becomes evanescent, traveling along the liquid surface. Such a configuration maximizes surface sensitivity. The dimension of the X-ray beam footprint on the liquid surface was approximately $2 \times 50\ mm^2$ and was bigger than the width of the ultra-small volume Langmuir trough we used. This caused over illumination of the sample and small increases in the scattering background. The scattered intensity was measured by scanning over a range of horizontal scattering vectors, Q_{xy}, the combination of horizontal components Q_x and Q_y (49, 50). Bragg peaks are intensity resolved in the Q_{xy}-direction and integrated over channels along the z-direction in the position sensitive detector. The position of the maxima of the Bragg peaks, Q_{xy}^{max}, was used to calculate the repeat distances $d = 2\pi/Q_{xy}$ of the 2D lattice. The widths of the peaks, corrected for the instrument resolution, were used to determine the 2D crystalline in-plane coherence length, L_{xy} (the average distance in the direction of the reciprocal lattice vector Q_{xy} over which there is “near-perfect” crystallinity).

Neutron reflectivity measurements

Neutron reflectometry (NR) experiments were performed on hTau40 associated with supported lipid bilayers using the Surface ProfilE Analysis Reflectometer, or SPEAR, at Los Alamos National Lab (55). Methods and measurement of NR using SPEAR have been previously described (56). In general, lipid bilayers were created using a Langmuir-Blodgett/Langmuir-Schaefer deposition method. 1 mg/mL DMPG in 9:1 $CHCl_3$:MeOH and DPPC in $CHCl_3$ were used as spreading solutions. Lipids were spread at the air-water interface in a Langmuir trough and compressed to a target pressure of 25 or 40 mN/m. A quartz substrate was drawn through the air-water interface to deposit the first layer, then rotated and driven back through the interface to deposit the second layer. A solid-liquid interface cell was then assembled (Fig. 1C) and purged with D_2O. After collecting NR data of the pure lipid bilayer, which takes about an hour and half, an aliquot of 5 μM hTau40 in deuterated PBS was injected into the flow cell, allowed to equilibrate for 20 minutes, and NR data were collected again.

Neutrons entered the lateral face of the substrate and were scattered from the substrate-subphase interface (Fig. 1C). D_2O provided scattering contrast between the substrate, hydrogen-rich bilayer, and subphase. Similar contrast conditions can also be obtained by using deuterated lipids in a subphase of H_2O but no additional information relevant to this publication can be obtained by performing NR measurements in both the contrast conditions. Therefore NR measurements were performed on hydrogenated lipid bilayers in a D_2O subphase. During the experiments, the ratio of elastically scattered to incident neutrons, or reflectivity (R), was measured as a function of the momentum-transfer vector Q_z. Analysis of the NR data provided information about coherent scattering-length density (SLD) distribution normal to the sample.

SLD is a value unique to a particular chemical composition and is the sum of coherent scattering lengths of constituent elements divided by the volume that they occupy. The continuous function SLD often can be well approximated by a number of layers, or boxes, each with a constant and distinct SLD. Inter-layer roughness can be taken into account using an error function centered at each interface (33). The incident neutron beam is refracted at each interface and a theoretical NR curve can be calculated using the Parratt recursion formula (57). The measured and theoretical NR curves are compared, and using genetic optimization and the Levenburg-Marquardt nonlinear least-squares method, the best least-squares fit, corresponding to the lowest χ^2 value, is obtained (58). The simplest SLD model that gave good fits of physical relevance was used to interpret the NR data.

Results

Surface activity of hTau40

With the aim of understanding tau interaction with lipid membranes, we first assessed tau's inherent propensity to exhibit exogenous interactions by measuring its surface activity. Experimentally, surface pressure (π) reached by the adsorption of hTau40 to the air/water interface from a water subphase was measured. As shown by the adsorption isotherm in Fig. 2, hTau40 rapidly adsorbed to the air/water interface after its injection into the subphase, with no lag time, and reached an equilibrium π of ~ 16 mN/m. Strikingly, this π value reached by the highly charged and soluble tau is comparable to that reached by the amphiphilic Aβ peptide (45, 55). Moreover, the adsorption isotherm showed a two-stage behavior where π initially increased sharply to about 9 mN/m, followed by a plateau and subsequent slowed increase to achieve a final π of 16 mN/m. This adsorption experiment was repeated and the two-stage adsorption behavior was found to be reproducible. However, this adsorption behavior was not observed for other proteins under identical experimental

conditions and procedures (46, 54) indicating that the two-stage behavior is not due to experimental artifacts, such as mixing effects, but rather, reflects a protein specific effect, possibly structural rearrangements of the protein layer following the rapid adsorption of the protein to the air/water interface.

The XR data obtained for hTau40 at the air/water interface and the corresponding model independent and box model fitted electron density profiles (ρ, normalized to water, ρ/ρ_{H_2O}) are shown in Fig. 3. Box model fitting parameters for the X-ray reflectivity data are summarized in Table 1. Two boxes of disparate electron densities gave the best fit to the XR data, indicating inhomogeneity of the surface adsorbed tau film in the direction perpendicular to the air/water interface. A more dense ~8 Å portion with $\rho/\rho_{H2O} = 1.29$ is formed at the hydrophobic air phase, followed by a more diffuse layer with ρ close to that of water ($\rho/\rho_{H2O} \approx 1$) that extends another 8 Å into the water subphase. GIXD data of the film did not show any diffraction peaks (data not shown) indicating a lack of long-range ordering, in the plane of the film, for hTau40 adsorbed at the air/water interface.

hTau40 insertion into lipid monolayers

Isotherms and the accompanying percent trough area expansion of hTau40 insertion into DMPC, DMPG, and DMTAP monolayers are shown in Fig. 4. Time zero of the area expansion corresponds to the time of tau injection into the water subphase. The small degrees of contraction for the DMPC and DMTAP films observed immediately after injection of the protein are likely due to the perturbation to the films from sample injection. As previously described, a feedback loop is utilized to maintain constant surface pressure. When the film is perturbed, the barriers move to compensate for fluctuations in monolayer pressure. This is supported by the observation that contraction is larger for more fluid films, whereas the primarily condensed DMPG monolayer did not show any contraction upon injection. Because of this, the initial contractions seen in our data are likely experimental artifacts.

The protein did not insert into the zwitterionic DMPC monolayer held at 25 mN/m and only inserted when π was step-wise lowered to 16 mN/m (Fig. 4A). Since this π coincided with hTau40's equilibrium adsorption π (Fig. 2), our data indicate that hTau40 did not exhibit favorable interactions with the neutral DMPC membrane. In contrast, when injected underneath the anionic DMPG monolayer held at 25 mN/m, hTau40 inserted into the monolayer and caused an area expansion of 91%. When injected underneath the cationic DMTAP monolayer held at 25 mN/m, hTau40 inserted into the monolayer after a short delay, but only resulted in an 8.5% area expansion (Fig. 4B).

Disruption of the DMPG monolayer induced by hTau40 insertion was assessed by monitoring the morphology of the lipid film before and after hTau40 injection. Representative FM images are shown in Fig. 5. At 25 °C, the DMPG monolayer on water undergoes a liquid-expanded (LE) to liquid-condensed (LC) phase transition at ~17 mN/m as indicated by the plateau in the DMPG isotherm in Fig. 4A. Because the bulky lipid dye molecules, TR-DHPE, are preferentially excluded from the ordered LC phase, it appears as dark domains in FM whereas the fluid LE phase containing the dyes is bright. Fig. 5A shows that at 25 mN/m, the DMPG monolayer contains predominantly the LC phase. Ten minutes after the injection of hTau40 (~5% area expansion), the general appearance of the LC domains changed from a well-defined circular shape to one that is less well-defined, indicative of decreased line tension around the LC domains due to the association of the tau protein to the lipid monolayer (Fig. 5B). Additionally, the ratio of dark to light regions is reduced. These changes in the monolayer morphology became more pronounced with continued insertion of hTau40, where, in addition to decreased dark to light regions, the dark LC domains also became smaller, pointing to the disruption of these ordered domains.

X-ray scattering measurements of hTau40 associated with lipid monolayers

GIXD data of hTau40 associated with a DMPG monolayer showed that the insertion of tau disrupted the ordered packing of lipid tails (Fig. 6), in agreement with observed disruption to monolayer morphology observed by FM (Fig. 5). The DMPG monolayer at 25 mN/m showed a single Bragg peak, consistent with the LC domains observed from FM. The Q_{xy} position of the peak maximum at 1.483 $Å^{-1}$ corresponds to a d-spacing of 4.237 Å and a 2D hexagonal unit cell dimension, a_h, of 4.893 Å. The area per DMPG molecule is 41.47 $Å^2$ and the average size of the ordered domains is ~270 Å. After the insertion of hTau40, no diffraction peaks were observed in the monolayer (Fig. 6), indicating that the ordered lipid phase had been disrupted by the insertion of the tau protein. Moreover, tau associated with the DMPG monolayer did not give rise to any scattering peaks (data not shown), indicating that the protein did not fold and assemble into in-plane crystalline structures detectable by GIXD.

XR profiles of tau-associated with DMPG monolayer exhibited significant differences compared to that of lipids alone (Fig. 7A). XR data of the DMPG monolayer before and at two different time points (t1 and t2) after the injection of hTau40 are shown for comparison. Qualitatively, reflectivity of the DMPG film alone showed the characteristic “two humps” of the lipid monolayer, one corresponding to the lipid headgroups and the second to the alkyl tails. After the injection of tau, significant differences in the reflectivity were observed in a time-dependent manner. Minima in the reflectivity curves became shallower and the overall intensity of the signals decreased.

Analysis of the XR data using the StochFit (53) yielded ρ/ρ_{H_2O} distributions perpendicular to the protein/lipid film (Fig. 7B). Box model fitting parameters are summarized in Table 1. A two box model fit of the DMPG lipids alone shows a region of high ρ corresponding to lipid headgroups and a region of lower ρ corresponding to lipid acyl tails (see top schematic in Fig. 7B). With the insertion of hTau40, three boxes were required to provide good fits to the two XR data sets, t1 and t2. The box at the air interface with ρ/ρ_{H_2O} values close to 0.9 corresponds to DMPG tail groups and this box decreased in thickness with tau insertion. The box corresponding to the headgroup region of DMPG increased in thickness and slightly decreased in ρ/ρ_{H_2O} with hTau40 insertion. Additionally, a region of slightly higher ρ compared to ρ_{H_2O} adjacent to the DMPG headgroups on the subphase side was required to fit the data. These physical changes to the DMPG film taken together indicate the presence of protein both in the head group and tail regions of the lipid monolayer, as well as a diffuse layer of protein underneath the head groups (see middle and bottom schematics in Fig. 7B). The middle layer thus encompasses a portion of lipid tails, lipid head groups, and protein, all of which contribute to the overall ρ/ρ_{H_2O} fitted for this layer. Lipid tails, which have significantly lower electron density, most likely caused the decreases in the electron density of this middle layer as more of the tail region became incorporated into this layer. Thus, XR measurements revealed that hTau40 inserted into the DMPG monolayer was located: 1. underneath the lipid headgroups, 2. in the charged headgroup region, and 3. partially in the hydrophobic tail region. With time, the tau protein penetrated further into the hydrophobic tail region. The three modes of interaction gave rise to a ~20 Å thick protein layer at the membrane surface with the portion of the protein that had intercalated into the lipid membrane exhibiting a ρ/ρ_{H_2O} of ~1.3.

Neutron reflectivity measurements of hTau40 associated with supported lipid bilayers

Figs. 8 and 9 summarize the NR data and fitted SLD profiles obtained before and after the injection of hTau40 into the flow cells containing supported DPPC and DMPG lipid bilayers, respectively. DPPC was chosen instead of the more fluid DMPC to obtain a more stable bilayer vis-à-vis the solid support. Additionally, both DPPC and DMPG bilayers are

in the condensed phase at the surface pressure and temperature used for the experiments, whereas DMPC would be in the fluid phase. Thus, DPPC and DMPG bilayers used in this study are valid membranes for comparing the effect of lipid membrane charge while maintaining the same membrane phase state.

Similar to the XR data, the NR results are normalized by Fresnel to highlight important features. Intact bilayers are indicated by a distinctive “two-hump” pattern, with each peak representing an intact monolayer, whereas bilayers that have been disrupted lack these two peaks (Fig. 9C). Figure 8 shows the NR and corresponding SLD profile for a DPPC bilayer, deposited at a lipid monolayer pressure of 25 mN/m before (Figs. 8A and 8B) and after (Figs. 8C and 8D) the injection of hTau40 in the subphase. Cartoon depictions for these two cases are also shown. Our data show that the addition of hTau40 did not have any effect on the DPPC membrane structure. In contrast, the addition of hTau40 completely disrupted a DMPG bilayer deposited at 40 mN/m (Figs. 9C and 9D). A similar effect was observed for a DMPG bilayer deposited at 25 mN/m (data not shown). The parameters used for fitting the data shown in Figures 8 and 9 are summarized in Table 2. The higher SLD of the tail region for DMPG bilayer deposited at 25 and 40 mN/m, as compared to the SLD of the tail region for DPPC bilayer, signifies the presence of some D_2O in the modeled tail region of the DMPG bilayer.

Discussion

hTau40 is highly surface active

Although highly charged and soluble, the full-length human hTau40 exhibits significant surface activity, adsorbing readily to the air/water interface to give a final π comparable to that reached by the adsorption of the amphipathic Aβ40 peptide to an air/water interface (46). The intrinsically disordered, or “soft” nature, of the tau protein thus renders it highly surface active, prone to partition or bind to different interfaces. The initial sharp increase in π (Fig. 2) is indicative of hTau40's high affinity to the hydrophobic interface and the reproducible two-stage adsorption behavior suggests that the protein undergoes structural rearrangements once adsorbed to the interface. The specific nature of this structural rearrangement is at present unclear. The lack of GIXD diffraction peaks from this interface adsorbed tau film indicates that no long range repeat structures in the plane of the film, e.g., the repeat β-sheets in amyloid protofibrils or fibrils (54), are formed at the air/water interface. This, however, does not preclude the formation of local, non-prorogating, secondary structures or amorphous tau aggregates at the air/water interface.

hTau40 selectively interacts with anionic membranes

To understand the role lipid membranes play in mediating the dynamics of hTau40, we investigated the interactions between two types of model lipid membranes and hTau40. The Langmuir monolayer is used to model one leaflet of the plasma membrane, while the supported lipid bilayers provide a better model of the plasma membrane. As demonstrated by the monolayer insertion assays, hTau40 strongly associated and inserted into the anionic DMPG monolayer, presumably in part mediated by the attractive electrostatic interactions between the positively charged MT binding domain of hTau40 (Fig. 1A) and the lipids. The strong affinity of the MT binding domain with anionic membranes is also in agreement with previous reports on the tau repeat domain construct (K18), which forms the core of the paired-helical filaments, aggregating in the presence of anionic lipid vesicles (21). Tau also favorably interacted with positively charged DMTAP membrane, presumably through its negatively charged projection N-terminus, but inserted to a much lesser extent compared to DMPG. hTau40 did not exhibit any favorable interactions with the neutral DMPC lipids. The selective affinity of hTau40 towards anionic membranes is further evidenced by the

complete disruption of a supported anionic DMPG bilayer while leaving zwitterionic DPPC bilayer intact (Figs. 8 and 9). Our findings suggest that electrostatic interactions play an important role in modulating tau-membrane interactions, with hTau40 displaying a strong affinity toward the anionic DMPG membrane. However, the extent of tau interaction with membranes could be mediated by additional factors, as evidenced by the disparate extents of insertion into anionic and cationic membranes. Further investigations utilizing different tau constructs will help to clarify the importance of these factors.

Air/water and lipid membrane interfaces induce tau structural compaction

The tau film adsorbed to the air/water interface is about 20 Å thick and is not homogeneous in its electron density distribution perpendicular to the film surface (Fig. 3). A more dense ~10 Å layer with a ρ/ρ_{H_2O} of 1.3 is formed at the hydrophobic air phase, followed by a more diffuse layer with a ρ/ρ_{H_2O} close to 1 that extends further into the water phase. XR data modeling of tau inserted into a DMPG monolayer (Fig. 7) shows that the membrane association and partial insertion of tau into the lipid headgroup and tail regions gave rise to a ~10 Å layer of protein in the membrane with a ρ/ρ_{H_2O} of about 1.3 (Fig. 7B), followed by a more diffuse layer underneath the DMPG head groups with a ρ/ρ_{H_2O} close to 1 that extends into the water phase. The radius of gyration (R_g) of the intrinsically disordered hTau40 in solution (determined by small-angle X-ray scattering) has been reported to be 65 Å (59), much larger than a globular, folded protein of ~400 amino acids with R_g typically ranging from 20-25 Å. Furthermore, a ρ/ρ_{H_2O} of 1.3 of the more dense portion of hTau40 layers at the air/water and membrane interfaces is comparable to the density of folded proteins that have an average specific volume of 0.73, which corresponds to a density of 1.37 g/ml (60).

Taken together, our structural measurements of air/water interface-adsorbed and membrane interface-associated tau layers of a smaller dimension and higher density compared to tau in solution suggest that as the intrinsically disordered tau partitions to interfaces, at least a portion of the protein undergoes structural compaction to resemble the density of a folded protein. This conformational change may also be accompanied by protein-protein interactions that lead to amorphous aggregation of tau at the interfaces. In light of previous reports on the ability of anionic membranes to induce tau fibrillization (15, 21), the anionic membrane induced structural compaction of hTau40 elucidated here provides the molecular basis of early structural changes that can then lead to fibrillization. Structurally compacted conformations of the full-length tau protein that exhibit enhanced aggregation propensity have been shown in several cases, including phosphorylation at several sites diagnostic of AD (61, 62), binding to exogenous aggregation inducers (63), and fast heating/cooling (64). We show here that the binding of tau to two different interfaces, a hydrophobic interface (the air/water interface) and a physiological membrane interface, can also induce structural compaction. Our data, along with previous reports, clearly demonstrate the structural plasticity of the tau protein and that multiple mechanisms can induce structural compaction that accompanies disordered-to-order transitions in the protein to render it aggregation-competent. However, the exact conformation tau adopts in the interfacial films is not clear. These tau films appear to be amorphous in long-range order, as no ordered crystalline domains were detectable by GIXD. But the lack of long-range order does not preclude the formation of local, whether intramolecular or intermolecular, secondary structures, which can render the otherwise soluble and stable tau to misfold into a conformation that is “pro-aggregant” or aggregation-competent.

hTau40 association with membranes disrupts lipid packing and membrane integrity

Morphological changes to the DMPG lipid monolayer caused by the insertion of tau were observed by FM. As previously shown in Aβ-membrane studies (46, 65), disruption to monolayer morphology can be indicative of disruption to lipid packing. An overall increase

in the ratio of light LE phase to dark LC phase can be caused by preferential insertion of hTau40 into the more fluid LE region and/or disruption of the ordered LC domains. The change of LC domain shape and decrease of the size of these domains indicate that hTau40 insertion disrupts lipid packing in the LC domains. This disruption is corroborated by our GIXD data, where on the molecular level, hTau40 insertion into DMPG monolayer completely disrupted the ordered packing of lipid tails.

NR experiments used to assess lipid bilayer structural integrity before and after the addition of hTau40 showed that tau selectively disrupted anionic DMPG lipid bilayers even at lipid packing densities higher than those of a cell membrane. Tau disrupted DMPG bilayers deposited at both 25 and 40 mN/m. In contrast, the neutrally charged DPPC bilayer was not affected by the addition of tau. This result is in agreement with results from lipid monolayer insertion assay where hTau40 did not exhibit any favorable interactions with the neutral DMPC monolayer. Our results thus confirm that hTau40 preferentially interacts with anionic membranes, not only with a DMPG monolayer at the air-water interface, but also with more physiologically relevant lipid bilayers. Moreover, these interactions disrupt lipid membrane structure, both on a molecular scale of disrupting lipid packing and on a morphological scale of completely disrupting the integrity of lipid bilayers.

Conclusions

Our results provide some structural insights into the dual roles that the lipid membrane plays in catalyzing tau misfolding and aggregation and in serving as a target for tau aggregates to exert toxicity *via* membrane destabilization. *In vitro*, tau aggregation requires the addition of exogenous polyanionic cofactors. We examine here the interaction of tau with the more physiological lipid membrane and the effect of these interactions on tau conformation and membrane structural integrity. The “soft nature” of the protein gives rise to a high surface activity as evidenced by tau's strong affinity to adsorb to the hydrophobic air/water interface. Tau also has a strong tendency to associate with and intercalate into negatively charged lipid monolayers and bilayers. Both interfaces induced the intrinsically disordered hTau40 to partially adopt a more compact conformation similar to that of a folded protein. Since anionic membranes have been shown to induce tau fibrillization, this lipid membrane-induced structural compaction may render the otherwise soluble and stable tau aggregation-competent, or pro-aggregant, and seed the assembly of tau into fibrils. The inner leaflet of neuronal cell membrane contains several anionic lipid species. Upon the detachment of tau from microtubules due to hyperphosphorylation that occurs early on during the pathogenesis of Alzheimer's disease, association of free tau with anionic lipids in the plasma membrane can seed the formation of PHFs. Furthermore, tau's interaction with anionic lipid membranes disrupted lipid packing and compromised membrane structural integrity, suggesting a mechanism of protein aggregate-induced toxicity in diseased cells.

Acknowledgments

We gratefully acknowledge support from the Alzheimer's Association, UNM Research Allocation Committee, and Oak Ridge Associated Universities. EMJ acknowledges fellowship support from the NSF-IGERT program “Integrative Nanoscience and Microsystems” and the NCI Alliance for Nanotechnology in Cancer. EM and JB acknowledge support from the Max-Planck-Society and Volkswagen Foundation. This work benefited from the use of the Lujan Neutron Scattering Center at LANSCE funded by the DOE Office of Basic Energy Sciences and Los Alamos National Laboratory under DOE Contract DE-AC52-06NA25396 and the BW1 Beamline and Dr. Bernd Struth at the Deutsches Elektronen-Synchrotron in Hamburg, Germany.

REFERENCES

1. Soto C. Unfolding the role of protein misfolding in neurodegenerative diseases. Nat Rev Neurosci. 2003; 4:49–60. [PubMed: 12511861]

2. Buée L, Bussière T, Buée-Scherrer V, Delacourte A, Hof PR. Tau protein isoforms, phosphorylation and role in neurodegenerative disorders. Brain Research Reviews. 2000; 33:95–130. [PubMed: 10967355]
3. Selkoe D. Toward a Comprehensive Theory for Alzheimer's Disease. Hypothesis: Alzheimer's Disease Is Caused by the Cerebral Accumulation and Cytotoxicity of Amyloid β-Protein. Annals of the New York Academy of Sciences. 2000; 924:17–25. [PubMed: 11193794]
4. Kosik KS, Joachim CL, Selkoe DJ. Microtubule-associated protein tau (tau) is a major antigenic component of paired helical filaments in Alzheimer disease. Proceedings of the National Academy of Sciences. 1986; 83:4044–4048.
5. Lee VMY, Goedert M, Trojanowski JQ. Neurodegenerative Tauopathies. Annual Review of Neuroscience. 2001; 24:1121–1159.
6. Berger Z, Roder H, Hanna A, Carlson A, Rangachari V, Yue M, Wszolek Z, Ashe K, Knight J, Dickson D, Andorfer C, Rosenberry TL, Lewis J, Hutton M, Janus C. Accumulation of Pathological Tau Species and Memory Loss in a Conditional Model of Tauopathy. The Journal of Neuroscience. 2007; 27:3650–3662. [PubMed: 17409229]
7. Poorkaj P, Bird TD, Wijsman E, Nemens E, Garruto RM, Anderson L, Andreadis A, Wiederholt WC, Raskind M, Schellenberg GD. Tau is a candidate gene for chromosome 17 frontotemporal dementia. Ann Neurol. 1998; 43:815–825. [PubMed: 9629852]
8. Spillantini MG, Goedert M. Tau protein pathology in neurodegenerative diseases. Trends in Neurosciences. 1998; 21:428–433. [PubMed: 9786340]
9. Weingarten MD, Lockwood AH, Hwo SY, Kirschner MW. A protein factor essential for microtubule assembly. Proceedings of the National Academy of Sciences. 1975; 72:1858–1862.
10. Cleveland DW, Hwo S-Y, Kirschner MW. Physical and chemical properties of purified tau factor and the role of tau in microtubule assembly. Journal of Molecular Biology. 1977; 116:227–247. [PubMed: 146092]
11. Goedert M, Jakes R, Spillantini MG, Hasegawa M, Smith MJ, Crowther RA. Assembly of microtubule-associated protein tau into Alzheimer-like filaments induced by sulphated glycosaminoglycans. Nature. 1996; 383:550–553. [PubMed: 8849730]
12. Wilson DM, Binder LI. Free fatty acids stimulate the polymerization of tau and amyloid beta peptides. In vitro evidence for a common effector of pathogenesis in Alzheimer's disease. American Journal of Pathology. 1997; 150:2181–2195. [PubMed: 9176408]
13. King ME, Gamblin TC, Kuret J, Binder LI. Differential Assembly of Human Tau Isoforms in the Presence of Arachidonic Acid. Journal of Neurochemistry. 2000; 74:1749–1757. [PubMed: 10737634]
14. Barghorn S, Mandelkow E. Toward a Unified Scheme for the Aggregation of Tau into Alzheimer Paired Helical Filaments†. Biochemistry. 2002; 41:14885–14896. [PubMed: 12475237]
15. Chirita C, Necula M, Kuret J. Anionic Micelles and Vesicles Induce Tau Fibrillization in Vitro. Journal of Biological Chemistry. 2003; 278:25644–25650. [PubMed: 12730214]
16. Brandt R, Léger J, Lee G. Interaction of tau with the neural plasma membrane mediated by tau's amino-terminal projection domain. The Journal of Cell Biology. 1995; 131:1327–1340. [PubMed: 8522593]
17. Kawarabayashi T, Shoji M, Younkin LH, Wen-Lang L, Dickson DW, Murakami T, Matsubara E, Abe K, Ashe KH, Younkin SG. Dimeric Amyloid β Protein Rapidly Accumulates in Lipid Rafts followed by Apolipoprotein E and Phosphorylated Tau Accumulation in the Tg2576 Mouse Model of Alzheimer's Disease. The Journal of Neuroscience. 2004; 24:3801–3809. [PubMed: 15084661]
18. Williamson R, Usardi A, Hanger DP, Anderton BH. Membrane-bound β-amyloid oligomers are recruited into lipid rafts by a fyn-dependent mechanism. The FASEB Journal. 2008; 22:1552–1559.
19. Gray EG, Paula-Barbosa M, Roher A. Alzheimer's disease: paired helical filaments and cytomembranes. Neuropathol Appl Neurobiol. 1987; 13:91–110. [PubMed: 3614544]
20. Campos-Peña V, Tapia-Ramírez J, Sánchez-Torres C, Meraz-Rios MA. Pathological-Like Assembly of tau Induced by a Paired Helical Filament Core Expressed at the Plasma Membrane. Journal of Alzheimer's Disease. 2009; 18:919–933.

21. Elbaum-Garfinkle S, Ramlall T, Rhoades E. The Role of the Lipid Bilayer in Tau Aggregation. Biophysical Journal. 2010; 98:2722–2730. [PubMed: 20513417]
22. Lovestone S, McLoughlin DM. Protein aggregates and dementia: is there a common toxicity? Journal of Neurology, Neurosurgery & Psychiatry. 2002; 72:152–161.
23. Gendron TF, Petrucelli L. The role of tau in neurodegeneration. Molecular Neurodegeneration. 2009; 4:13. [PubMed: 19284597]
24. Deshpande A, Win KM, Busciglio J. Tau isoform expression and regulation in human cortical neurons. The FASEB Journal. 2008; 22:2357–2367.
25. Sydow A, Van der Jeugd A, Zheng F, Ahmed T, Balschun D, Petrova O, Drexler D, Zhou L, Rune G, Mandelkow E, D'Hooge R, Alzheimer C, Mandelkow EM. Tau-Induced Defects in Synaptic Plasticity, Learning, and Memory Are Reversible in Transgenic Mice after Switching Off the Toxic Tau Mutant. Journal of Neuroscience. 2011; 31:2511–2525. [PubMed: 21325519]
26. Conway KA, Lee S-J, Rochet J-C, Ding TT, Williamson RE, Lansbury PT. Acceleration of oligomerization, not fibrillization, is a shared property of both α-synuclein mutations linked to early-onset Parkinson's disease: Implications for pathogenesis and therapy. Proceedings of the National Academy of Sciences. 2000; 97:571–576.
27. Lashuel HA, Petre BM, Wall J, Simon M, Nowak RJ, Walz T, Lansbury PT Jr. [alpha]-Synuclein, Especially the Parkinson's Disease-associated Mutants, Forms Pore-like Annular and Tubular Protofibrils. Journal of Molecular Biology. 2002; 322:1089–1102. [PubMed: 12367530]
28. Walsh DM, Klyubin I, Fadeeva JV, Cullen WK, Anwyl R, Wolfe MS, Rowan MJ, Selkoe DJ. Naturally secreted oligomers of amyloid [beta] protein potently inhibit hippocampal long-term potentiation in vivo. Nature. 2002; 416:535–539. [PubMed: 11932745]
29. Sharon R, Bar-Joseph I, Frosch MP, Walsh DM, Hamilton JA, Selkoe DJ. The Formation of Highly Soluble Oligomers of [alpha]-Synuclein Is Regulated by Fatty Acids and Enhanced in Parkinson's Disease. Neuron. 2003; 37:583–595. [PubMed: 12597857]
30. Novitskaya V, Bocharova OV, Bronstein I, Baskakov IV. Amyloid Fibrils of Mammalian Prion Protein Are Highly Toxic to Cultured Cells and Primary Neurons. Journal of Biological Chemistry. 2006; 281:13828–13836. [PubMed: 16554307]
31. Kayed R, Sokolov Y, Edmonds B, McIntire TM, Milton SC, Hall JE, Glabe CG. Permeabilization of lipid bilayers is a common conformation-dependent activity of soluble amyloid oligomers in protein misfolding diseases. J Biol Chem. 2004; 279:46363–46366. [PubMed: 15385542]
32. Quist A, Doudevski I, Lin H, Azimova R, Ng D, Frangione B, Kagan B, Ghiso J, Lal R. Amyloid ion channels: a common structural link for protein-misfolding disease. Proc Natl Acad Sci U S A. 2005; 102:10427–10432. [PubMed: 16020533]
33. Chi EY, Ege C, Winans A, Majewski J, Wu G, Kjaer K, Lee KY. Lipid membrane templates the ordering and induces the fibrillogenesis of Alzheimer's disease amyloid-beta peptide. Proteins. 2008; 72:1–24. [PubMed: 18186465]
34. Chi EY, Frey SL, Lee KYC. Ganglioside GM1-Mediated Amyloid-beta Fibrillogenesis and Membrane Disruption. Biochemistry. 2007; 46:1913–1924. [PubMed: 17256880]
35. Demuro A, Mina E, Kayed R, Milton SC, Parker I, Glabe CG. Calcium dysregulation and membrane disruption as a ubiquitous neurotoxic mechanism of soluble amyloid oligomers. J Biol Chem. 2005; 280:17294–17300. [PubMed: 15722360]
36. Deshpande A, Mina E, Glabe C, Busciglio J. Different conformations of amyloid beta induce neurotoxicity by distinct mechanisms in human cortical neurons. J Neurosci. 2006; 26:6011–6018. [PubMed: 16738244]
37. Simakova O, Arispe NJ. The cell-selective neurotoxicity of the Alzheimer's Abeta peptide is determined by surface phosphatidylserine and cytosolic ATP levels. Membrane binding is required for Abeta toxicity. J Neurosci. 2007; 27:13719–13729. [PubMed: 18077683]
38. Sun XD, Mo ZL, Taylor BM, Epps DE. A slowly formed transient conformer of A beta(1-40) is toxic to inward channels of dissociated hippocampal and cortical neurons of rats. Neurobiology of Disease. 2003; 14:567–578. [PubMed: 14678772]
39. Arispe N, Pollard HB, Rojas E. Giant Multilevel Cation Channels Formed by Alzheimer-Disease Amyloid Beta-Protein [a-Beta-P-(1-40)] in Bilayer-Membranes. P Natl Acad Sci USA. 1993; 90:10573–10577.

40. Arispe N, Pollard HB, Rojas E. The ability of amyloid beta-protein [A beta P (1-40)] to form Ca2+ channels provides a mechanism for neuronal death in Alzheimer's disease. Ann N Y Acad Sci. 1994; 747:256–266. [PubMed: 7847675]
41. Sokolov Y, Kozak JA, Kayed R, Chanturiya A, Glabe C, Hall JE. Soluble amyloid oligomers increase bilayer conductance by altering dielectric structure. J Gen Physiol. 2006; 128:637–647. [PubMed: 17101816]
42. Valincius G, Heinrich F, Budvytyte R, Vanderah DJ, McGillivray DJ, Sokolov Y, Hall JE, Losche M. Soluble amyloid beta-oligomers affect dielectric membrane properties by bilayer insertion and domain formation: implications for cell toxicity. Biophys J. 2008; 95:4845–4861. [PubMed: 18515395]
43. Gidalevitz D, Ishitsuka Y, Muresan AS, Konovalov O, Waring AJ, Lehrer RI, Lee KYC. Interaction of antimicrobial peptide protegrin with biomembranes. Proceedings of the National Academy of Sciences. 2003; 100:6302–6307.
44. Wang Y, Tang Y, Zhou Z, Ji E, Lopez GP, Chi EY, Schanze KS, Whitten DG. Membrane Perturbation Activity of Cationic Phenylene Ethynylene Oligomers and Polymers: Selectivity against Model Bacterial and Mammalian Membranes. Langmuir. 2010; 26:12509–12514. [PubMed: 20586429]
45. Gustke N, Trinczek B, Biernat J, Mandelkow EM, Mandelkow E. Domains of tau protein and interactions with microtubules. Biochemistry. 1994; 33:9511–9522. [PubMed: 8068626]
46. Ege C, Lee KYC. Insertion of Alzheimer's A[beta]40 Peptide into Lipid Monolayers. Biophysical Journal. 2004; 87:1732–1740. [PubMed: 15345552]
47. Seelig A. Local anesthetics and pressure: a comparison of dibucaine binding to lipid monolayers and bilayers. Biochimica et Biophysica Acta (BBA) - Biomembranes. 1987; 899:196–204.
48. Knobler CM. Seeing Phenomena in Flatland: Studies of Monolayers by Fluorescence Microscopy. Science. 1990; 249:870–874. [PubMed: 17773103]
49. Als-Nielsen, J.; Kjaer, K. X-ray reflectivity and diffraction studies of liquid surfaces and surfactant monolayers. In: Riste, T.; Sherrington, D., editors. The proceedings of the Nato Advanced Study Institute, Phase transitions in soft condensed Matter. Plenum Press; Geilo, Norway: 1989. p. 113-137.
50. Als-Nielsen J, Jacquemain D, Kjaer K, Leveiller F, Lahav M, Leiserowitz L. Principles and applications of grazing incidence X-ray and neutron scattering from ordered molecular monolayers at the air-water interface. Physics Reports. 1994; 246:251–313.
51. Jensen, TR.; Kjaer, K. Structural properties and interactions of thin films at the air-liquid interface explored by synchrotron X-Ray scattering. In: Möbius, D.; Miller, R., editors. Studies in Interface Science. Elsevier; 2001. p. 205-254.
52. Pedersen JS, Hamley IW. Analysis of Neutron and X-Ray Reflectivity Data by Constrained Least-Squares Methods. Physica B. 1994; 198:16–23.
53. Danauskas SM, Li D, Meron M, Lin B, Lee KYC. Stochastic fitting of specular X-ray reflectivity data using StochFit. Journal of Applied Crystallography. 2008; 41:1187–1193.
54. Chi EY, Frey SL, Winans A, Lam KLH, Kjaer K, Majewski J, Lee Ka Yee C. Amyloid-[beta] Fibrillogenesis Seeded by Interface-Induced Peptide Misfolding and Self-Assembly. Biophysical Journal. 2010; 98:2299–2308. [PubMed: 20483339]
55. Dubey M, Jablin M, Wang P, Mocko M, Majewski J. SPEAR — ToF neutron reflectometer at the Los Alamos Neutron Science Center. The European Physical Journal Plus. 2011; 126:1.
56. Dubey M, Jablin MS, Smith H, Majewski J. Investigations of surrogate cellular membranes using neutron reflectometry. Acta Crystallographica Section D. 2010; 66:1237–1243.
57. Parratt LG. Surface Studies of Solids by Total Reflection of X-Rays. Phys Rev. 1954; 95:359–369.
58. Nelson A. Co-refinement of multiple-contrast neutron/X-ray reflectivity data using MOTOFIT. J Appl Crystallogr. 2006; 39:273–276.
59. Bernadó P, Mylonas E, Petoukhov MV, Blackledge M, Svergun DI. Structural Characterization of Flexible Proteins Using Small-Angle X-ray Scattering. Journal of the American Chemical Society. 2007; 129:5656–5664. [PubMed: 17411046]
60. Lee JC, Timasheff SN. Partial specific volumes and interactions with solvent components of proteins in guanidine hydrochloride. Biochemistry. 1974; 13:257–265. [PubMed: 4855654]

61. Jeganathan S, von Bergen M, Mandelkow E-M, Mandelkow E. The Natively Unfolded Character of Tau and Its Aggregation to Alzheimer-like Paired Helical Filaments†. Biochemistry. 2008; 47:10526–10539. [PubMed: 18783251]

62. Jeganathan S, von Bergen M, Brutlach H, Steinhoff H-J, Mandelkow E. Global Hairpin Folding of Tau in Solution†. Biochemistry. 2006; 45:2283–2293. [PubMed: 16475817]

63. Chirita CN, Congdon EE, Kuret J. Triggers of full-length tau aggregation: a role for partially folded. Biochemistry. 2005; 44:5862–5872. [PubMed: 15823045]

64. Shkumatov AV, Chinnathambi S, Mandelkow E, Svergun DI. Structural memory of natively unfolded tau protein detected by small-angle X-ray scattering, Proteins: Structure. Function, and Bioinformatics. 2011; 79:2122–2131.

65. Bokvist M, Lindström F, Watts A, Gröbner G. Two Types of Alzheimer's [beta]-Amyloid (1-40) Peptide Membrane Interactions: Aggregation Preventing Transmembrane Anchoring Versus Accelerated Surface Fibril Formation. Journal of Molecular Biology. 2004; 335:1039–1049. [PubMed: 14698298]

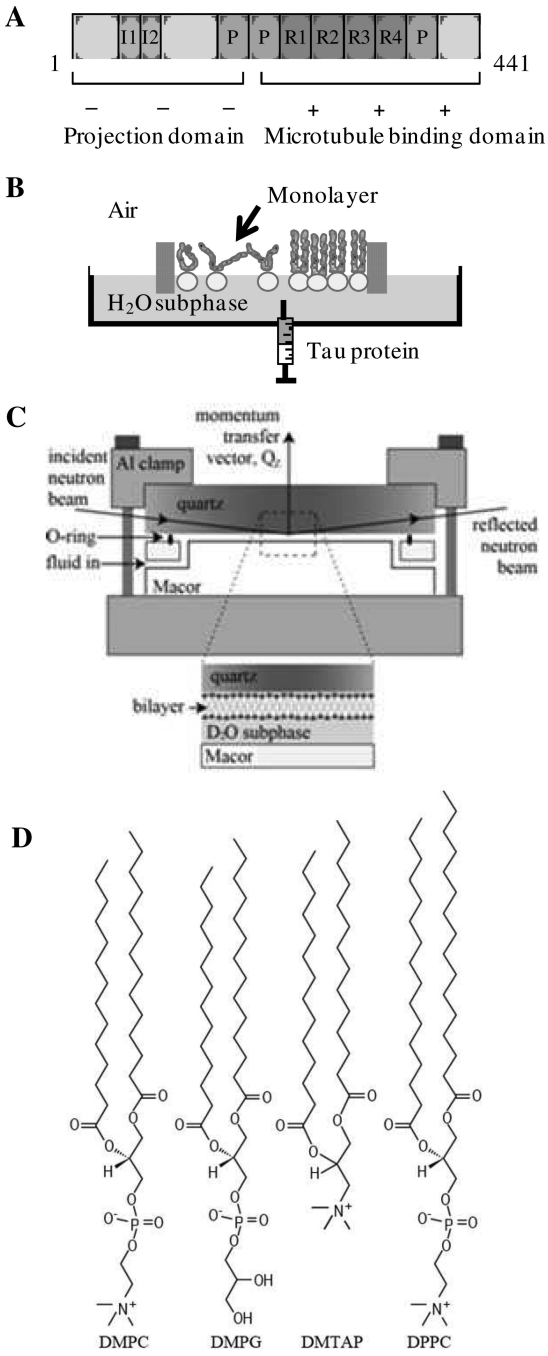

Figure 1.

Schematics of (A) hTau40 indicating projection and microtubule binding domains and their overall charge states, (B) Langmuir trough containing a lipid monolayer for protein insertion assays, (C) solid-liquid interface cell used in neutron scattering experiments, and (D) lipids used in monolayer and bilayer experiments. The DMPC, DMPG and DMTAP lipids have identical 14-carbon acyl chains but differ in their head group architecture and charge. DPPC and DMPC have the same neutral head group, but DPPC has 16-carbon tails.

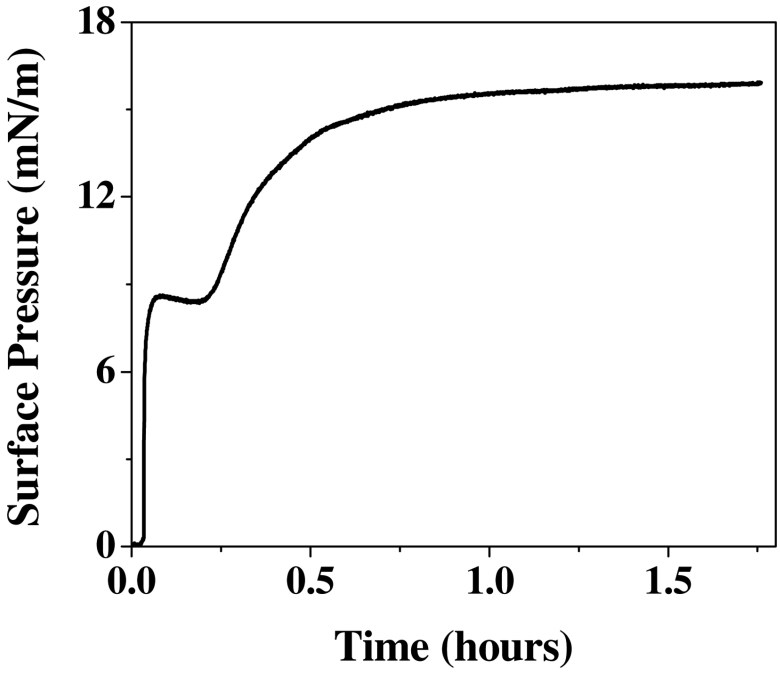

Figure 2.
Adsorption isotherm of hTau40 to an air/water interface at 25°C and 1 μM.

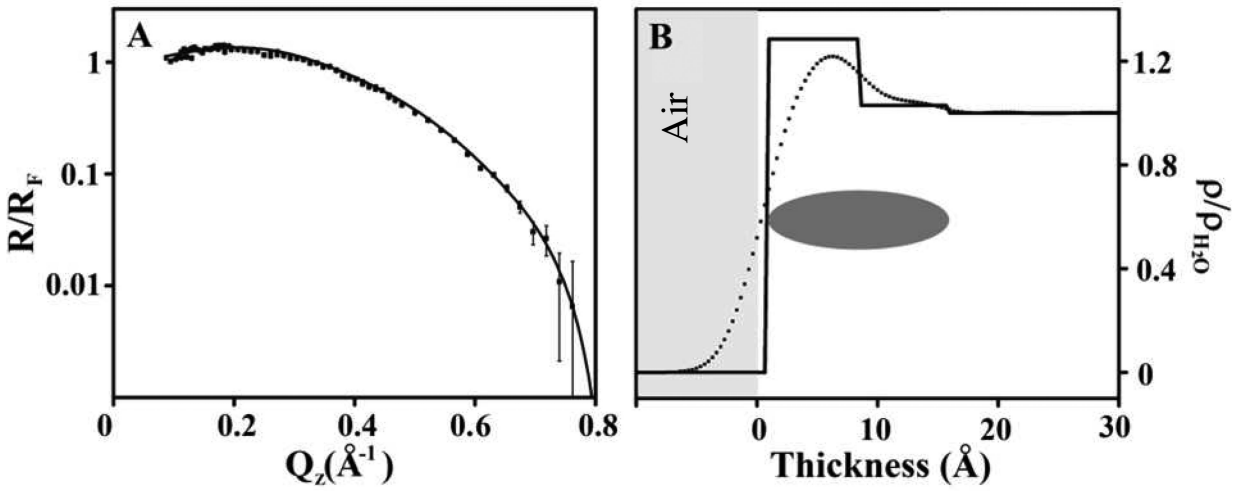

Figure 3.

(A) Fresnel normalized X-ray reflectivity (R/R_F) and (B) water normalized electron density (ρ/ρ_{H_2O}) of hTau40 adsorption to the air/water interface at 23 °C and 1 μM. The dashed line indicates a model independent fit and the solid line indicates a box-model fit. A schematic indicating the location of the hTau40 is also included. Thickness value 0 corresponds to air/protein interface where negative values indicate the air phase.

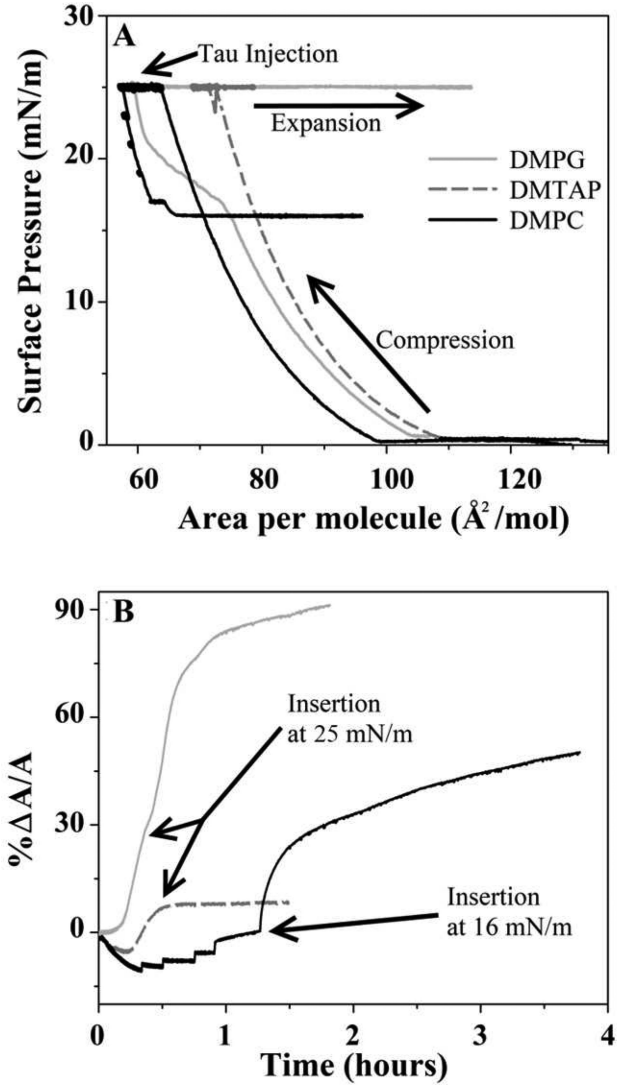

Figure 4.

Isotherms (A) and corresponding percent area expansion profiles (B) for hTau40 insertion into DMPG (gray solid line), DMTAP (dashed line), and DMPC (black solid line) monolayers at 25°C on water subphase. The lipid monolayers were first compressed to 25 mN/m, after which tau was injected into the subphase. Time zero in the area expansion profiles (B) corresponds to the time of injection of protein. No insertion was observed at 25 mN/m for DMPC. Pressure was reduced stepwise until insertion was observed at 16 mN/m. Tau spontaneously inserted into DMPG and DMPTAP monolayers at 25 mN/m.

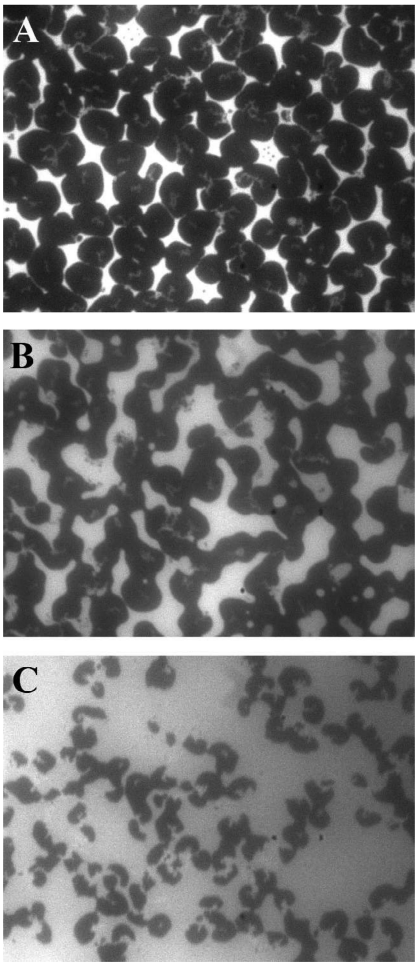

Figure 5.
FM images of a DMPG lipid monolayer during hTau40 insertion. Images were collected (A) before tau injection, and (B) 10 and (C) 30 minutes after injection, corresponding to ~ 5% and 14% area expansion, respectively.

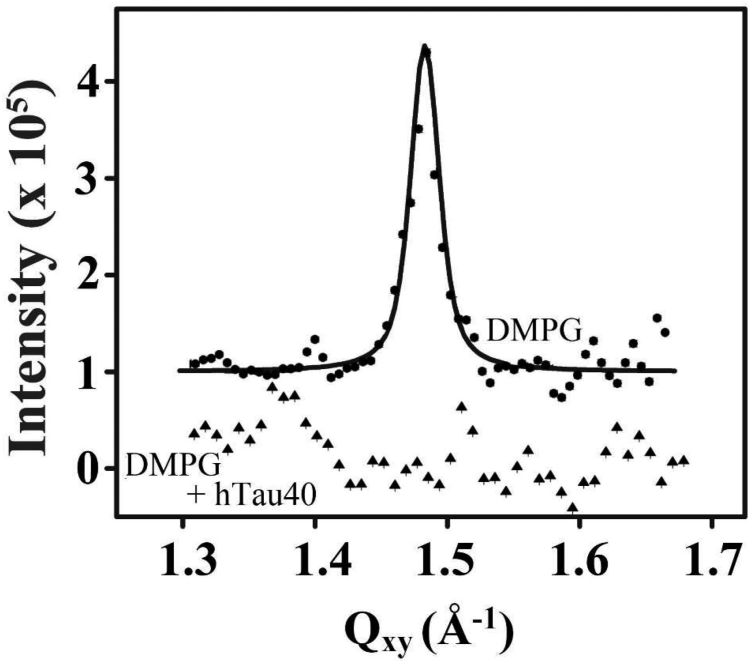

Figure 6.

Background subtracted GIXD data of DMPG (filled circles) and DMPG/tau (filled triangles) monolayers at 23 °C. The DMPG monolayer at 25 mN/m showed a single Bragg peak whereas no peaks were observed from the DMPG/tau film. Data are offset for clarity.

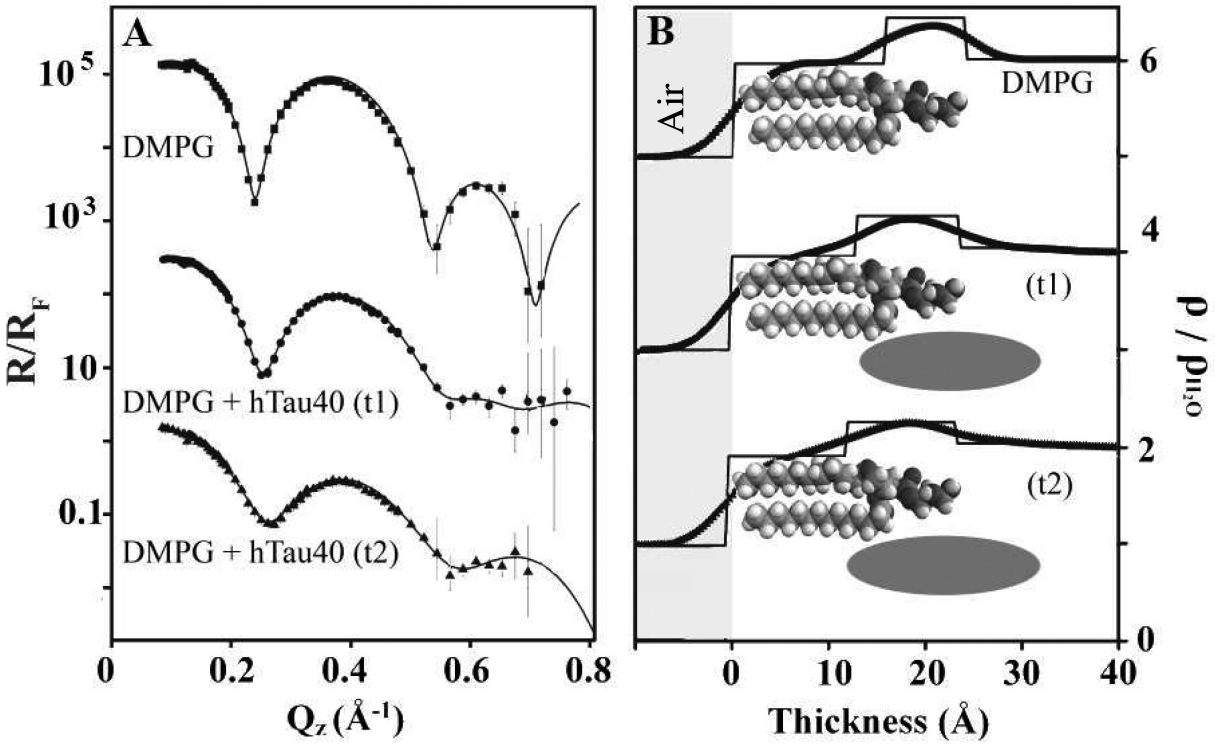

Figure 7.

(A) Fresnel normalized X-ray reflectivity (R/R_F) and (B) water normalized electron density (ρ/ρ_{H_2O}) of DMPG monolayer before and at two time points (t1 and t2) after the injection of hTau40 into the subphase. A: Model independent fits (lines) to R/R_F data (filled symbols) from Stochfit. B: ρ/ρ_{H_2O} profiles from model independent fits (curved line profiles) and box model fits (straight line profiles). Data for both reflectivity and electron density are offset for clarity. The reflectivity value for bare DMPG is offset by 1000 and t1 is offset by 10. The electron density for DMPG is offset by 5, for t1 by 3, and for t2 by 1. Schematics depicting location of lipids and tau are also shown. Thickness value 0 corresponds to air/lipid tail interface where negative values indicate the air phase.

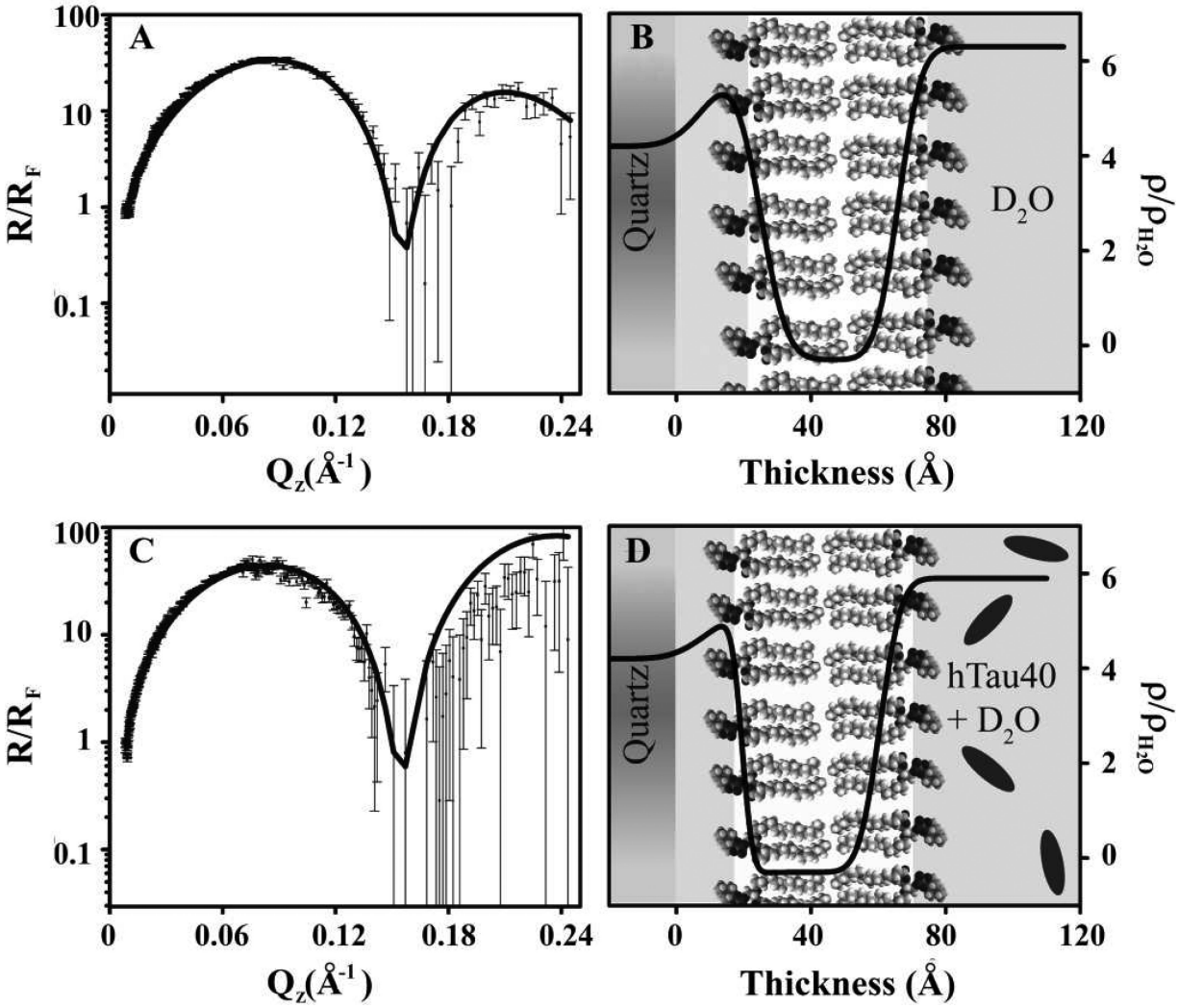

Figure 8.

Fresnel normalized neutron reflectivity (R/R_F) (A and C) and corresponding SLD profiles (B and D) for a DPPC bilayer deposited onto a quartz substrate at 25 mN/m before (A and B) and after (C and D) after tau addition. The lines are the fitted NR and SLD profiles. Schematics depicting lipids and proteins are also included.

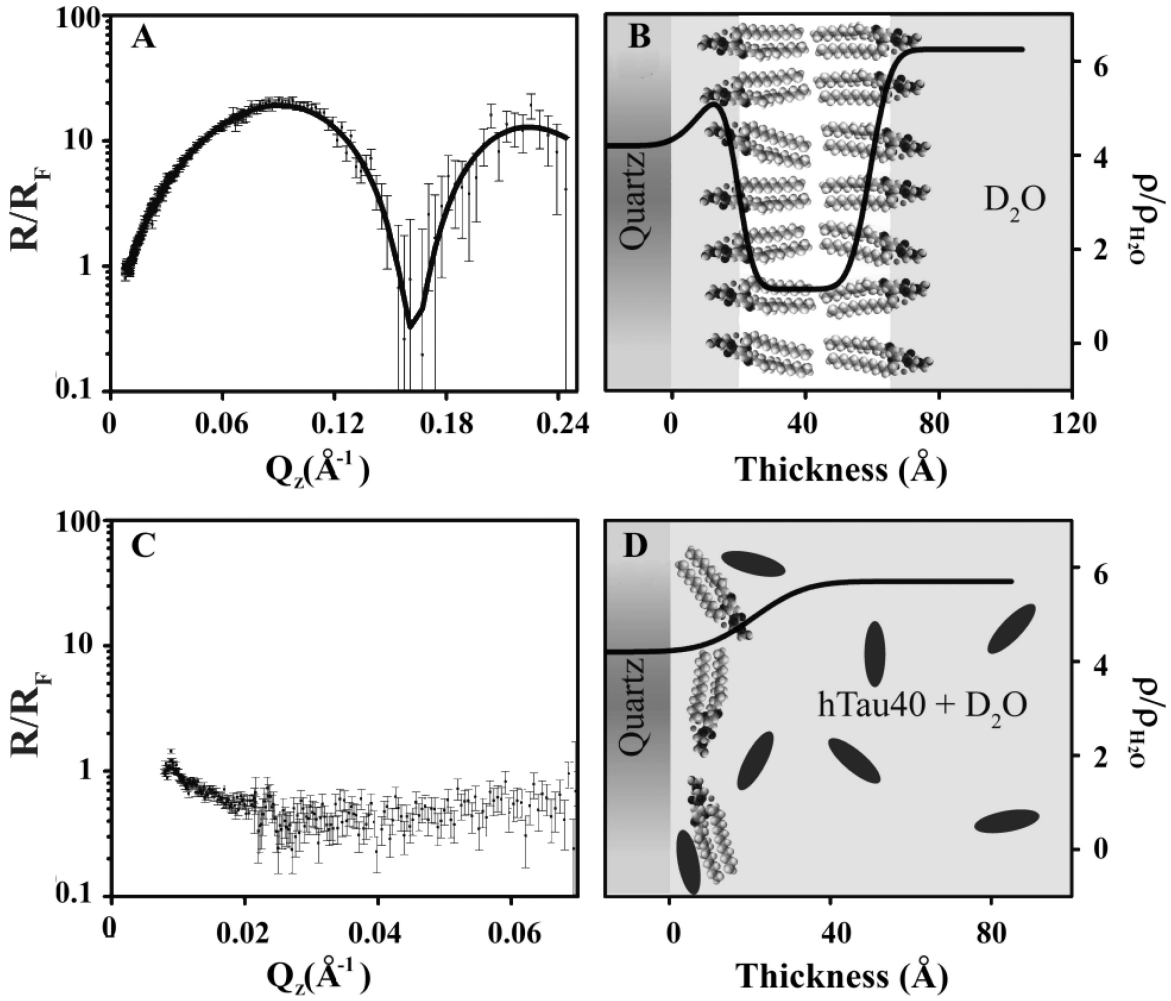

Figure 9.

Fresnel normalized neutron reflectivity (R/R_F) (A and C) and corresponding SLD profiles (B and D) for a DMPG lipid bilayer deposited onto a quartz substrate at 40 mN/m before (A and B) and after (C and D) tau addition. The lines are the fitted NR and SLD profiles. Schematics depicting lipids and proteins are also included.

Table 1

X-ray Reflectivity Box Fit Parameters. Errors reported are standard deviations obtained from the non-linear least square fitting of the reflectivity data with box models using the Levenberg-Marquadt algorithm (53).

Sample	Box Composition	Thickness (Å)	ρ/ρ_{H2O}	Roughness (Å)
hTau40	Air/protein interface	7.99 ± 2.4E-2	1.27 ± 4.8E-3	2.66 ± 1.5E-3
	Protein/subphase interface	7.93 ± 5.6E-2	1.02 ± 3.9E-3	2.37 ± 4.7E-4
DMPG	Lipid tails	14.9 ± 4.3E-2	0.94 ± 1.1E-2	3.11 ± 1.3E-3
	Lipid heads	9.78 ± 8.1E-2	1.37 ± 1.4E-2	2.91 ± 3.7E-3
DMPG + hTau40 t1	Lipid tails	13.4 ± 5.2E-1	0.93 ± 1.4E-1	2.96 ± 5.3E-2
	Lipid tails + heads + hTau40	10.3 ± 1.2E-1	1.32 ± 1.6E-2	3.19 ± 4.9E-1
	hTau40	10.1 ± 1.2E0	1.01 ± 2.9E-2	3.33 ± 6.1E-1
DMPG + hTau40 t2	Lipid tails	12.3 ± 6.5E-2	0.91 ± 1.7E-2	3.25 ± 3.1E-1
	Lipid tails + heads + hTau40	11.2 ± 1.8E-1	1.25 ± 2.1E-2	3.25 ± 1.1E0
	hTau40	9.01 ± 3.7E-1	1.04 ± 2.7E-2	2.33 ± 7.8E-1

Table 2

Neutron Reflectivity Least-Squares Fit Parameters

Flow Cell Contents	Layer Composition	Thickness (Å)	SLD (10^{-6} Å^{-2})	Roughness (Å)
DPPC 25 mN/m	D_2O + DPPC heads	15.9	6.00	8.00
	DPPC tails	41.0	-0.300	6.15
DPPC 25 mN/m + hTau40	D_2O + DPPC heads	10.8	5.20	7.97
	DPPC tails	41.0	-0.300	2.48
DMPG 40 mN/m	D_2O + DMPG heads	10.9	5.64	6.82
	DMPG tails	39.7	1.15	3.82